

Neutron and X-Ray Powder Diffraction Studies of $\text{LiMn}_{2-y}\text{Cr}_y\text{O}_4$

K. Oikawa¹ and T. Kamiyama

Institute of Materials Science, University of Tsukuba, Tsukuba, Ibaraki 305-8573, Japan

F. Izumi

National Institute for Research in Inorganic Materials, Tsukuba, Ibaraki 305-0044, Japan

and

D. Nakazato, H. Ikuta, and M. Wakihara

Department of Chemical Engineering, Tokyo Institute of Technology, Ookayama, Meguro-ku, Tokyo 152-8552, Japan

Received January 26, 1999; in revised form April 13, 1999; accepted April 22, 1999

The crystal structures of chromium-doped spinel-type lithium manganese oxides, $\text{LiMn}_{2-y}\text{Cr}_y\text{O}_4$ ($y = 0, \frac{1}{6}, \frac{1}{3}$, and $\frac{1}{2}$), have been studied by neutron and X-ray powder diffraction. Rietveld refinements of their neutron diffraction data revealed that Cr is substituted for Mn selectively and that Li occupies only the 8a site. Thus, the above solid solutions can be expressed as $\text{Li}(\text{Mn}_{2-y}\text{Cr}_y)\text{O}_4$. The fractional coordinates of oxygen were almost the same in all the samples while the lattice parameter a decreased linearly with increasing Cr content. The lengths of (Mn, Cr)–O bonds in (Mn, Cr) O_6 octahedra changed in a manner expected from average ionic radii for $\text{Mn}_{2-y}\text{Cr}_y$. Rietveld analyses of the X-ray diffraction data showed the crystallite size and anisotropic strain to decrease with increasing Cr content.

© 1999 Academic Press

INTRODUCTION

The spinel-type lithium manganese oxide LiMn_2O_4 and its related materials have been studied extensively as potential candidates for cathode materials in rechargeable lithium-ion batteries (1). For the commercial use of the rechargeable battery, the total capacity after charge/discharge iterations over hundreds of times is important. An initial capacity of about 130 (mA h)/g, which is close to the theoretical value of 148 (mA h)/g, can be obtained with a $\text{Li}/\text{LiMn}_2\text{O}_4$ cell in a 4-V region, but its capacity fades rapidly during charge/discharge cycles.

Li-rich and quaternary spinel oxides $\text{LiMn}_{2-y}M_y\text{O}_4$ ($M = \text{Li}$ or 3d transition metals) have been investigated to

improve its cycling performance (2–8). In general, increasing the amount of substitution for Mn, y , decreases the initial capacity. Until recently, Li-rich manganese oxide had been regarded as the most attractive candidate because a very small amount of excess Li, for example, $y = 0.04$, makes cycle stability at room temperature much higher, whereas quaternary spinel phases required more substitution, e.g., $\frac{1}{6}$ for $M = \text{Co}$ or Cr (5). At present, fast capacity fading during charge/discharge cycling at relatively high temperature, e.g., 55°C, has been recognized as a more serious problem (8–10). The capacity retention of cells using Li-rich spinel oxides is, however, poor at high temperature, and the application of quaternary spinel phases is now being reconsidered widely. Among them, the highest total performance is achieved in a $\text{Li}/\text{LiMn}_{2-y}\text{Cr}_y\text{O}_4$ cell with $y = 0.012$ (8). Reasons for its stability against the capacity fading, in particular at high temperature, have been estimated by several workers (5, 6, 8) but unsettled as yet.

The crystal structures of $\text{LiMn}_{2-y}\text{Cr}_y\text{O}_4$ were studied only by X-ray diffraction despite the importance of their structural information (5, 6, 11–13). Rietveld refinement with X-ray diffraction data on the basis of cubic space group $Fd\bar{3}m$ (no. 227) gives only a lattice parameter a and an oxygen coordinate with a large estimated standard deviation (e.s.d.). Main questions concerning their crystal structures are as follows:

- (i) Are Cr atoms substituted for Mn atoms at the octahedral 16d site selectively?
- (ii) Do Li atoms occupy only the tetrahedral 8a site?
- (iii) Do O atoms fully occupy the 32e site?
- (iv) How do metal–oxygen bond lengths vary with the content of Cr?

¹ Present address: Advanced Science Research Center, Japan Atomic Energy Research Institute, Tokai, Naka-gun, Ibaraki 319-1195, Japan. Fax: +81-29-282-6716. E-mail: oikawa@kotai3.tokai.jaeri.go.jp.



Answers to these questions can hardly be derived from Rietveld refinement of X-ray diffraction data. In this study, we have applied both neutron and X-ray powder diffraction to $\text{LiMn}_{2-y}\text{Cr}_y\text{O}_4$ and obtained detailed information about their structural properties.

EXPERIMENTAL

Mn_2O_3 was produced by heating MnCO_3 (99.9%, Soekawa Chemicals) at 500°C for 24 h. $\text{LiMn}_{2-y}\text{Cr}_y\text{O}_4$ ($y = 0, \frac{1}{6}, \frac{1}{3},$ and $\frac{1}{2}$) were prepared by heating Li_2CO_3 (99%, Wako Pure Chemical Industries), Cr_2O_3 (special quality, Yoneyama Chemical Industries), and Mn_2O_3 at 700°C for 3 days in air with intermittent grinding and cooling slowly at a rate of 1°C/min (5, 14).

Neutron powder diffraction data of the four samples were measured at 295 K for ca. 10 h on the time-of-flight (TOF) neutron diffractometer Vega (15) at the pulsed spallation neutron facility KENS. The samples were contained in a cylindrical V cell 8 mm in diameter, 30 mm in height, and 25 μm in thickness. An array of 112 position-sensitive detectors (PSDs) installed in a backward bank with a 2θ range from 145° to 175° was used to collect the intensity data. Incident neutron spectra were monitored with a ^3He monitor counter. The difference in efficiency between the PSDs and the monitor counter was corrected using intensity data obtained in a separate measurement of incoherent scattering from V.

X-ray powder diffraction data of the four samples were measured at 295 K on a Rigaku RAD-C system with $\text{CuK}\alpha$ radiation monochromatized with curved graphite. Divergence and antiscatter slits of $\frac{1}{2}^\circ$ were selected to include the 111 reflection at $2\theta = 18.6^\circ$ (lattice-plane spacing, $d = 4.76 \text{ \AA}$), and a receiving slit of 0.15 mm to attain good resolution. The step width was set at 0.03° , which was close to $\frac{1}{3}$ of the minimum full-width at half maximum (fwhm) for the 111 reflection. The counting time per step was 10 s for all the samples.

RESULTS AND DISCUSSION

Neutron powder diffraction data in a d range from 0.45 to 3.20 \AA were analyzed by a Rietveld-refinement program RIETAN-98T for TOF neutron diffraction (16). An original technique called partial profile relaxation in RIETAN-98T was applied to 311, 400, 622, 731, and 553 reflections in all the samples, which lowered R_{wp} by 0.2–0.5%. Coherent scattering lengths used for the refinements were -1.90 fm (Li), -3.73 fm (Mn), 3.635 fm (Cr), and 5.803 fm (O) (17). X-ray powder diffraction data in a 2θ region from 12° to 120° were analyzed by another Rietveld-refinement program RIETAN-97 β for angle-dispersive diffraction (18). To attain better fitting for low-angle reflections, coefficients in Simpson's numerical integral to express profile asymmetry

(26) were slightly modified. Preferred orientation was not corrected in any of the refinements. All the e.s.d.'s of refinable structure parameters were calculated according to Scott's procedure (19), which afforded e.s.d.'s about three times as large as those evaluated with the conventional one.

In preliminary Rietveld refinements of the X-ray diffraction data, the occupancy, g , of Mn/Cr at the $8a$ and $16c$ sites proved to be negligible in all the samples. The X-ray diffraction patterns of samples with the nominal compositions LiMn_2O_4 and $\text{LiMn}_{5/3}\text{Cr}_{1/3}\text{O}_4$ showed them to contain two phases. In LiMn_2O_4 , the low-temperature phase (20) coexisted even at room temperature with a mass fraction of ca. 0.061(4). $\text{LiMn}_{5/3}\text{Cr}_{1/3}\text{O}_4$ was most likely composed of isotypic Cr-rich and Cr-poor cubic spinel phases, which will hereafter be referred to as α - and β -phases, respectively (see Fig. 1). Lattice parameters and mass fractions of 0.900(4) for the α -phase and 0.100 for the β -phase were determined by a multiphase Rietveld refinement. With a lattice parameter vs the Cr content curve in a range $0 \leq y \leq \frac{1}{6}$, the Cr content for the β -phase, y_β , was estimated to be 0.08 (see Fig. 2), and that for the α -phase, y_α , to be ca. 0.36, which was calculated with the equation $y_\alpha \times 0.900 + 0.08 \times 0.100 = \frac{1}{3}$.

Preliminary Rietveld refinements of the neutron diffraction data gave negligibly small occupation factors for Li at the $16c$ site. They were therefore fixed at zero for all the samples in subsequent refinements. The occupation factors of O at the $32e$ site, $g(\text{O})$, were also refined. The resulting occupancies were, for example, 0.982(17) for $y = \frac{1}{6}$ and 0.999(20) for $y = \frac{1}{9}$, which correspond to chemical formulas of $\text{LiMn}_{11/6}\text{Cr}_{1/6}\text{O}_{3.93(7)}$ and $\text{LiMn}_{17/9}\text{Cr}_{1/9}\text{O}_{4.00(8)}$, respectively. Though the oxygen site in the former sample appeared to be slightly deficient, $g(\text{O})$ is strongly correlated with other refinable parameters, in particular, a scale factor and atomic displacement parameters. The oxygen stoichiometry is affected by the calcination temperature and the rate of cooling (21, 22). Taking into account the heating temperature (700°C) and the very small cooling rate of 1°C/min on the synthesis of the present samples and the e.s.d.'s of $g(\text{O})$ very near to unity, we can safely conclude that the $32e$ site is fully occupied by O and fixed $g(\text{O})$ at unity for all the samples in subsequent refinements. The strong correlation and large e.s.d.'s may be ascribable to the large multiplicity of the O site. The occupation factors of Mn at the $16d$ site, $g(\text{Mn})$, were refined under a linear constraint of $g(\text{Cr}) = 1 - g(\text{Mn})$, and the converged value was, for example, 0.921(8) in the case of $y = \frac{1}{6}$, in accordance with the nominal value, $11/(6 \times 2) = 0.9167$, within the e.s.d. Then, $g(\text{Mn})$'s were fixed at the nominal values in final refinements. The mixed-metal $16d$ site will hereinafter be termed "B".

Figure 3 shows Rietveld-refinement patterns for the neutron diffraction data of $\text{LiMn}_{11/6}\text{Cr}_{1/6}\text{O}_4$. Weak reflections near 1.5, 1.6, 2.3, and 2.8 \AA were due to the Al wall of a sample chamber and excluded from the analyses. Table 1

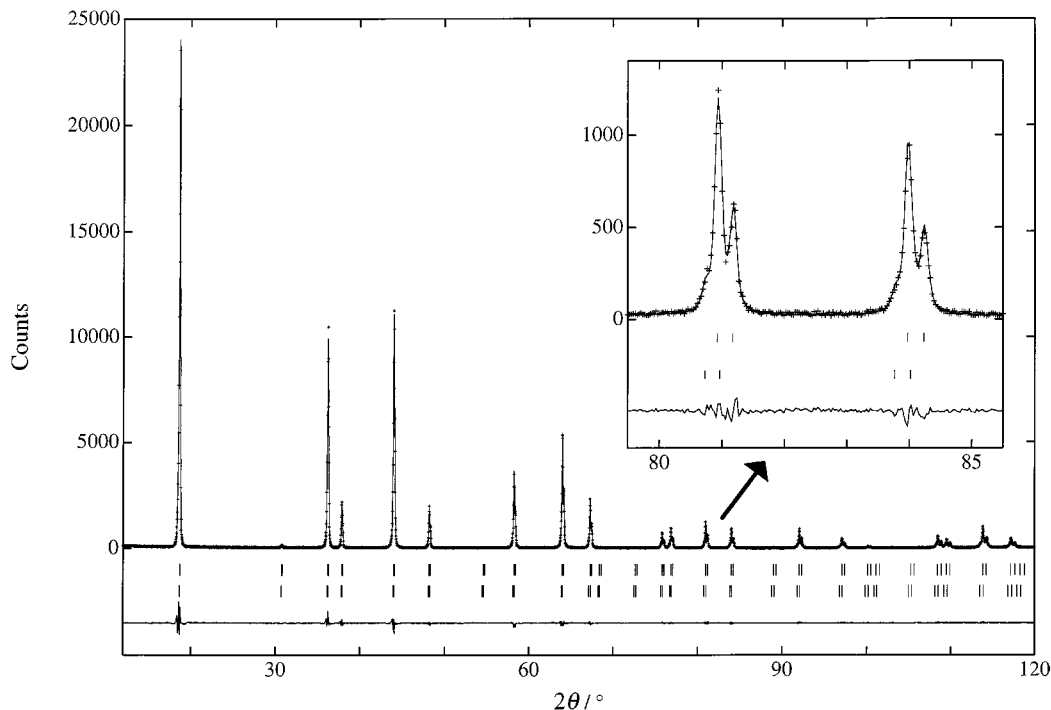


FIG. 1. Rietveld refinement patterns of $\text{LiMn}_{5/3}\text{Cr}_{1/3}\text{O}_4$ for the X-ray diffraction data taken at room temperature. Observed intensity data are shown by crosses, and the solid line overlying them is the calculated intensity. Vertical markers below the diffraction patterns indicate positions of possible Bragg reflections for the Cr-rich (upper) and Cr-poor (lower) phases. Differences between the observed and calculated intensities are plotted at the bottom in the same scale.

lists the final structure parameters obtained with the neutron diffraction data. The Li–O and B–O bond lengths, l , calculated with ORFFE (23) are given in Table 2 and plotted against y in Fig. 4. These bond lengths decreased linearly with increasing Cr content. Table 2 also lists $l_{\text{cal}}(\text{Li–O})$ and $l_{\text{cal}}(\text{B–O})$ calculated from the effective ionic radii of the Li^+ , Mn^{3+} , Mn^{4+} , and Cr^{3+} ions (24). The oxidation states of Mn, $+n$, were calculated on the basis of electrical neutrality and the assumption that the valence of

Cr is $+3$. Although $l_{\text{cal}}(\text{Li–O})$ did not change at all, $l(\text{Li–O})$ and $l(\text{Mn–O})$ varied in accordance with $l_{\text{cal}}(\text{B–O})$, which supports our structural model where the average oxidation state of Mn increases with increasing Cr content.

The diffraction patterns of $\text{LiMn}_{2-y}\text{Cr}_y\text{O}_4$ showed broadening of reflection profiles with its degree dependent on y . Then, we analyzed the profile broadening quantitatively with the X-ray powder diffraction data. The profile shape function adopted in RIETAN-97 β is the pseudo-Voigt function of Thompson, Cox, and Hastings (25) made asymmetric with Howard's procedure (26). The pseudo-Voigt function is calculated from U , V , W , and P for a Gaussian component and X , X_e , Y , and Y_e for a Lorentzian component (27, 28). X-ray diffraction data of NIST SRM 640b (Si) and SRM 674a (CeO_2 , Cr_2O_3 , Al_2O_3 , TiO_2 , and ZnO) were measured to evaluate profile parameters related to instrumental resolution: V , W , and Y . By careful Rietveld refinements of those standard samples, V and W were respectively found to be -1.7×10^{-3} and 1.34226×10^{-3} and fixed at these values in subsequent refinements (27). Y was estimated at 3.0×10^{-2} , which will be referred to as Y_{inst} in what follows. In the Rietveld refinements of $\text{LiMn}_{2-y}\text{Cr}_y\text{O}_4$, only U , X , and Y were varied. Anisotropic-broadening parameters for microstrain, Y_e , were also refined on the assumption that the anisotropic-broadening axis is $[100]$, whereas anisotropic Lorentzian

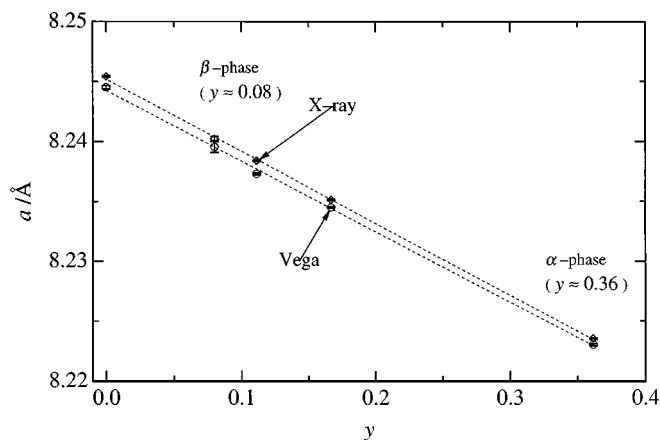


FIG. 2. Lattice parameter vs Cr content, y , in $\text{LiMn}_{2-y}\text{Cr}_y\text{O}_4$.

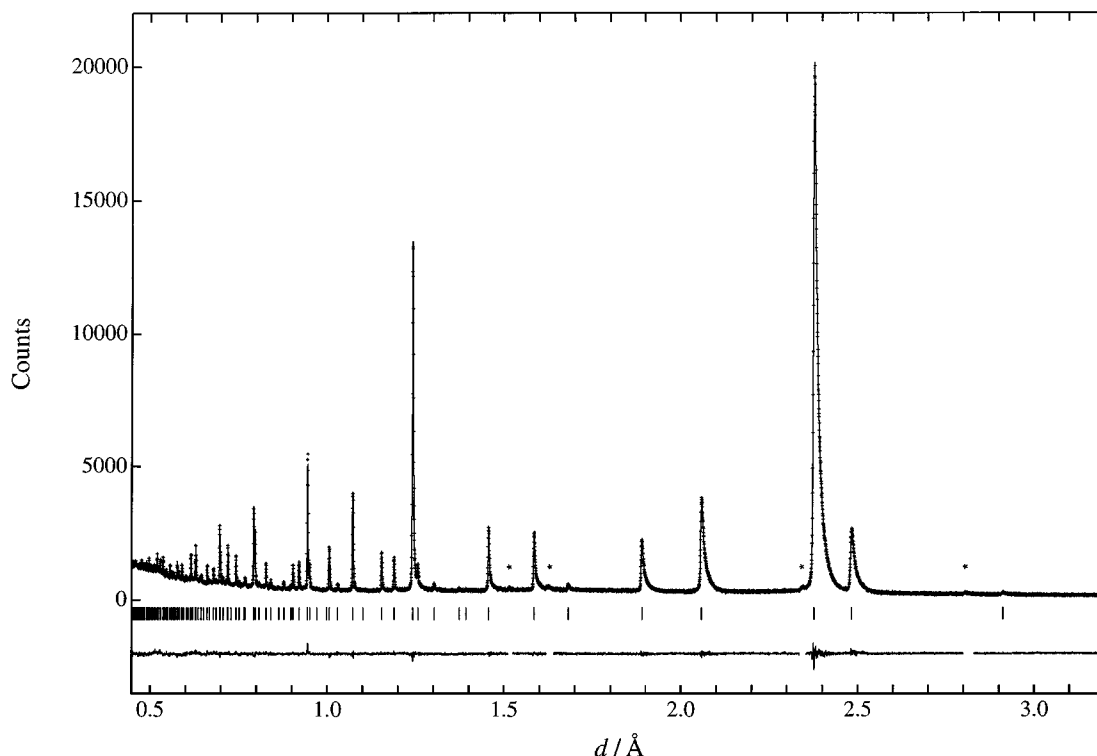


FIG. 3. Rietveld refinement patterns of $\text{LiMn}_{1.1/6}\text{Cr}_{1/6}\text{O}_4$ for the TOF neutron diffraction data measured at room temperature. TOF regions excluded from the Rietveld refinement are marked with asterisks.

Scherrer broadening parameters, X_e , were fixed at 0. Table 3 lists the final profile parameters and structure parameters obtained with the X-ray diffraction data.

The crystallite size, p , and anisotropic strain, S , in percentage points were calculated from refined profile parameters,

$$p \text{ (}\mu\text{m)} = \frac{180K}{\pi X} \times \frac{\lambda}{10000}, \quad [1]$$

$$S_{\parallel[100]} = \frac{\pi}{180} (Y + Y_e - Y_{\text{inst}}) \times 100, \quad [2]$$

$$S_{\perp[100]} = \frac{\pi}{180} (Y - Y_{\text{inst}}) \times 100, \quad [3]$$

where λ is the X-ray wavelength ($=1.540562 \text{ \AA}$) and $S_{\parallel[100]}$ and $S_{\perp[100]}$ are the components of strain parallel and perpendicular to the $[100]$ axis, respectively (27, 28). The Scherrer constant, K , was assumed to be unity. The resulting crystallite sizes and strains are plotted in Fig. 5.

Anisotropy in the profile broadening and p obviously decreased with increasing Cr content of the present sample. The crystallite size, which is inversely proportional to the

square root of the surface area, is regarded as one of the most critical parameters in preventing Mn dissolution (10), which mainly originates from the surface. The p values derived from the refined profile parameters suggest that substitution of Cr for Mn in a great degree is unfavorable for application to a cathode material because of the resultant decrease in crystallite size, i.e., the increase in surface area. To clear the relation between Cr content and crystallite size, more precise profile analysis as well as Rietveld refinement of diffraction data taken on the samples prepared by different conditions, e.g., different compositions and/or different calcination temperatures, is indispensable.

Anisotropic profile broadening mainly arises from elastic anisotropy and/or anisotropic internal stress. The elastic property will not vary very much by introducing a small amount of Cr. Then, the suppression of anisotropic broadening on Cr doping may be caused by the elastic anomaly near the phase-transition temperature (14), which drops drastically on Cr substitution. Anisotropic internal stress is also likely to remain near the phase transition, owing to the inhomogeneity of the transition temperature. In any of these cases, the stored elastic energy leads to the instability of the structure, degrading the cycle performance. A more detailed profile analysis of diffraction data taken near the phase-transition temperature is necessary to learn the origin of the anisotropic profile broadening.

TABLE 1
Structure Parameters of $\text{LiMn}_{2-y}\text{Cr}_y\text{O}_4$ Obtained by the Rietveld Refinements of the TOF Neutron Diffraction Data

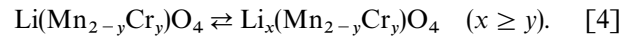
Atom	Site		$y = 0$	$y = \frac{1}{9}$	$y = \frac{1}{6}$	$y = \frac{1}{3}$
Li	8a	$x = y = z$	$\frac{1}{8}$	$\frac{1}{8}$	$\frac{1}{8}$	$\frac{1}{8}$
		$10^2 U_{11} (\text{\AA}^2)$	1.22(8)	1.07(24)	1.31(21)	1.07(9)
		$10^2 U_{12} (\text{\AA}^2)$	0	0	0	0
		$B_{\text{eq}} (\text{\AA}^2)$	0.964	0.848	1.035	0.847
		$g(\text{Cr})/g(\text{Mn})$	0	0.0556/0.9444	0.0833/0.9167	0.1807/0.8193
B	16d	$x = y = z$	$\frac{1}{2}$	$\frac{1}{2}$	$\frac{1}{2}$	$\frac{1}{2}$
		$10^2 U_{11} (\text{\AA}^2)$	0.86(6)	0.69(8)	0.82(7)	0.63(2)
		$10^2 U_{12} (\text{\AA}^2)$	-0.28(6)	-0.22(8)	-0.20(7)	-0.12(2)
		$B_{\text{eq}} (\text{\AA}^2)$	0.682	0.545	0.645	0.496
O	32e	$x = y = z$	0.26300(5)	0.26293(13)	0.26293(11)	0.26292(5)
		$10^2 U_{11} (\text{\AA}^2)$	1.67(6)	1.32(7)	1.40(5)	1.065(15)
		$10^2 U_{12} (\text{\AA}^2)$	-0.53(6)	-0.34(5)	-0.31(4)	-0.242(15)
		$B_{\text{eq}} (\text{\AA}^2)$	1.318	1.046	1.108	0.840
		R_{wp}	5.33%	5.53%	4.50%	4.72%
		R_{p}	3.93%	4.09%	3.29%	3.54%
		S	1.1012	1.1054	1.1301	1.1274
		R_{B}	2.49%	2.38%	2.44%	2.17%
		R_{F}	2.98%	2.60%	2.64%	2.29%

Note. U_{ij} 's are anisotropic atomic displacement parameters when the displacement factor is expressed as $\exp[-2\pi^2(h^2U_{11} + k^2U_{22} + l^2U_{33} + 2hkU_{12} + 2hlU_{13} + 2klU_{23})/a^2]$ with $U_{11} = U_{22} = U_{33}$ and $U_{12} = U_{13} = U_{23} = 0 \text{ \AA}^2$ for Li and $U_{11} = U_{22} = U_{33}$ and $U_{12} = U_{13} = U_{23}$ for B and O. B_{eq} is the equivalent isotropic atomic displacement parameter. Numbers in parentheses following refined parameters represent the e.s.d.'s of the last significant digit(s).

^aStructure parameters and phase-dependent R values, R_{B} and R_{F} , were calculated for the dominant Cr-rich phase assuming that $y = 0.3615$.

As described above, Cr atoms are substituted for Mn atoms selectively. Because the oxidation state of Cr remains unchanged in the 4-V region of the $\text{Li}/\text{LiMn}_{2-y}\text{Cr}_y\text{O}_4$ cell (13, 29), the ideal reversible reaction during the charge/dis-

charge processes can be represented as [4]:



Yamada (30) reported that the fading of capacity for the $\text{Li}/\text{LiMn}_2\text{O}_4$ cell in the 4-V region was promoted not by iterations in a deep-discharge region but by those in a deep-

TABLE 2
Lattice Parameters, a , and Metal–Oxygen Distances, l , in $\text{LiMn}_{2-y}\text{Cr}_y\text{O}_4$

	$y = 0$	$y = \frac{1}{9}$	$y = \frac{1}{6}$	$y = \frac{1}{3}^b$
a (Å)	8.24376(13)	8.23741(10)	8.23451(7)	8.22315(8)
$l(\text{Li–O})$	1.9706(7)	1.9680(19)	1.9672(15)	1.9644(8)
$l_{\text{cal}}(\text{Li–O})$	1.97	1.97	1.97	1.97
$l(\text{B–O})$	1.9598(3)	1.9586(10)	1.9580(8)	1.9553(4)
$l_{\text{cal}}(\text{B–O})^a$	1.9675	1.9658	1.9650	1.9621
Average Mn valence	3.5	3.529	3.546	3.610

^a $l_{\text{cal}}(\text{B–O})$ is the (Mn, Cr)–O distance calculated from effective ionic radii, r (24): $r(\text{Li}^+)$: 0.590 Å. $r(\text{Cr}^{3+})$: 0.615 Å. $r(\text{Mn}^{3+})$: 0.645 Å (high spin). $r(\text{Mn}^{4+})$: 0.530 Å. $r(\text{O}^{2-})$: 1.38 Å.

$$l_{\text{cal}}(\text{B–O}) = \frac{[y \times 0.615 + (1 - y) \times 0.645] + 0.530}{2} + 1.38 \text{ \AA}.$$

^bLattice parameter, metal–oxygen distances, and average Mn valence were calculated for the dominant Cr-rich phase assuming that $y = 0.3615$.

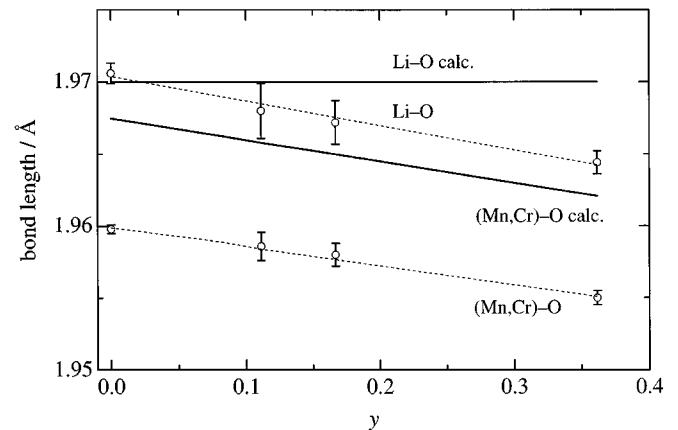


FIG. 4. B–O bond lengths in the BO_6 octahedron and Li–O bond lengths in the LiO_4 tetrahedron vs Cr content, y , in $\text{LiMn}_{2-y}\text{Cr}_y\text{O}_4$.

TABLE 3
Structure and Profile Parameters of $\text{LiMn}_{2-y}\text{Cr}_y\text{O}_4$ Obtained by the Rietveld Refinements of the X-Ray Diffraction Data

Atom	Site		$y = 0$	$y = \frac{1}{9}$	$y = \frac{1}{6}$	$y = \frac{1}{3}^a$
Li	8a	$x = y = z$	$\frac{1}{8}$	$\frac{1}{8}$	$\frac{1}{8}$	$\frac{1}{8}$
		$B (\text{\AA}^2)$	$= B(\text{O})$	$= B(\text{O})$	$B(\text{O})$	$= B(\text{O})$
		$g(\text{Cr})/g(\text{Mn})$	0	0.0556/0.9444	0.0833/0.9167	0.1807/0.8193
B	16d	$x = y = z$	$\frac{1}{2}$	$\frac{1}{2}$	$\frac{1}{2}$	$\frac{1}{2}$
		$B (\text{\AA}^2)$	0.80(2)	0.77(10)	0.67(10)	0.65(3)
O	32e	$x = y = z$	0.2630(2)	0.2633(8)	0.2631(8)	0.2637(3)
		$B (\text{\AA}^2)$	1.56(7)	1.4(3)	1.2(3)	1.04(8)
		$10^2 U$	0.0727(2)	0.19652(19)	0.05923(11)	0.15255(16)
		$10^2 X$	1.153(12)	1.686(11)	1.357(10)	2.196(11)
		$10^2 Y$	3.06(10)	3.56(9)	4.08(7)	5.06(8)
		$10^2 Y_c$	12.56(11)	9.12(9)	6.82(7)	3.66(8)
		R_{wp}	11.33%	10.71%	10.73%	10.23%
		R_p	7.58%	7.37%	7.12%	6.72%
		S	1.4768	1.4332	1.4038	1.3721
		R_B	2.63%	2.04%	1.54%	1.98%
		R_F	2.17%	1.62%	1.19%	1.31%

Note. B is the isotropic atomic displacement parameter. A linear constraint of $B(\text{Li}) = B(\text{O})$ were applied. Numbers in parentheses following refined parameters represent the e.s.d.'s of the last significant digit(s).

^a Structure parameters and phase-dependent R values, R_B and R_F , were calculated for the dominant Cr-rich phase assuming that $y = 0.3615$.

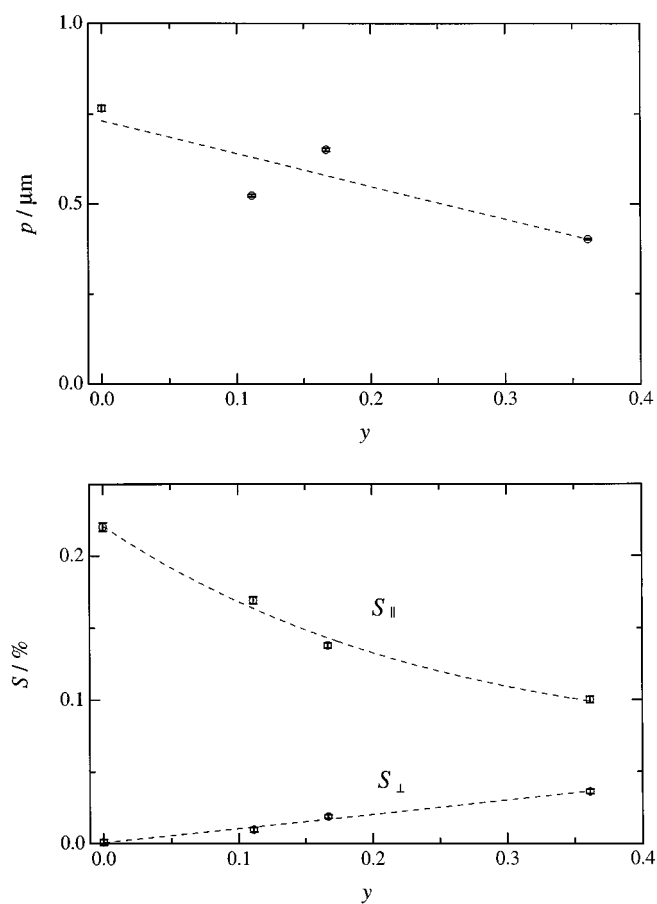
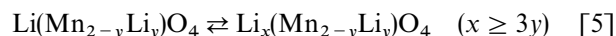


FIG. 5. Crystallite size and strain vs Cr content, y , in $\text{LiMn}_{2-y}\text{Cr}_y\text{O}_4$.

charge region where most Li^+ ions were deintercalated from the cathode material. The introduction of Cr^{3+} ions into the 16d positions stabilizes a network composed of $[\text{Mn}_{2-y}\text{Cr}_y]\text{O}_6$ octahedra over many cycles in the 4-V region because parts of Li^+ ions remain in the cathode. Similarly, the $\text{Li}/\text{Li}[\text{Mn}_{2-y}\text{Li}_y]\text{O}_4$ cell in which the reaction



proceeds instead of reaction [4] also exhibits good cycle performance for the same reason. In the fully charged state, the amount of remaining Li^+ ions in reaction [5] is three times as large as that in reaction [4] when y is the same. Therefore, substitution of Li with a y value greater than 0.05, which is required for capacity retention at high temperature, leads to a reduction in the initial capacity.

Robertson *et al.* (8) studied the cycle performance of an $\text{Li}/\text{LiMn}_{2-y}\text{Cr}_y\text{O}_4$ ($0 \leq y \leq 0.14$) cell in a 4-V region and concluded that the optimum composition was $\text{LiMn}_{1.988}\text{Cr}_{0.012}\text{O}_4$. The cycle performance vs y relation reported by them, however, seems to be somewhat inconsistent with that expected from our results; for example, the discharge capacity of $\text{Li}/\text{LiMn}_{1.98}\text{Cr}_{0.02}\text{O}_4$ is larger than that of $\text{Li}/\text{LiMn}_2\text{O}_4$ during all the cycles. The most probable reason for such a kind of inconsistency is inclusion of impurities. Close characterization of cathode materials is indispensable for understanding the cycle stability in such a region of low-level doping. In particular, structural properties such as those revealed in the present work are believed to affect the performance of Li-ion batteries.

REFERENCES

1. R. Koksang, J. Barker, H. Shi, and M. Y. Saidi, *Solid State Ionics* **84**, 1 (1996).
2. J. M. Tarascon, E. Wang, F. K. Shokoohi, W. R. McKinnon, and S. Colson, *J. Electrochem. Soc.* **138**, 2859 (1991).
3. R. J. Gummow, A. de Kock, and M. M. Thackeray, *Solid State Ionics* **69**, 59 (1994).
4. Y. Gao and R. Dahn, *J. Electrochem. Soc.* **143**, 100 (1996).
5. L. Guohua, H. Ikuta, T. Uchida, and M. Wakihara, *J. Electrochem. Soc.* **143**, 178 (1996).
6. G. Pistoia, A. Antonini, R. Rosati, C. Bellitto, and G. M. Ingo, *Chem. Mater.* **9**, 1443 (1997).
7. A. D. Robertson, S. H. Lu, W. F. Averill, and W. F. Howard, Jr., *J. Electrochem. Soc.* **144**, 3500 (1997).
8. A. D. Robertson, S. H. Lu, and W. F. Howard, Jr., *J. Electrochem. Soc.* **144**, 3505 (1997).
9. Y. Xia, Y. Zhou, and M. Yoshio, *J. Electrochem. Soc.* **144**, 2593 (1997).
10. G. G. Amatucci, C. N. Schmutz, A. Blyr, C. Sigala, A. S. Gozdz, D. Larcher, and J. M. Tarascon, *J. Power Sources* **69**, 11 (1997).
11. W. Baochen, X. Yongyao, F. Li, and Z. Dongjiang, *J. Power Sources* **43–44**, 539 (1993).
12. S. Kano and M. Sato, *Solid State Ionics* **79**, 215 (1995).
13. C. Sigala, A. Verbaere, J. L. Mansot, D. Guyomard, Y. Piffard, and M. Tournoux, *J. Solid State Chem.* **132**, 372 (1997).
14. D. Nakazato, M.Eng. thesis, Tokyo Institute of Technology, Tokyo, Japan, 1996.
15. T. Kamiyama, K. Oikawa, N. Tsuchiya, M. Osawa, H. Asano, N. Watanabe, M. Furusaka, S. Satoh, I. Fujikawa, T. Ishigaki, and F. Izumi, *Physica B* **213/214**, 1028 (1995).
16. T. Ohta, F. Izumi, K. Oikawa, and T. Kamiyama, *Physica B* **234–236**, 1093 (1997).
17. V. F. Sears, in "International Tables for Crystallography" (A. J. C. Wilson, Ed.), Vol. C, pp. 383–391. Kluwer, Dordrecht, 1992.
18. Y.-I. Kim and F. Izumi, *J. Ceram. Soc. Jpn.* **102**, 401 (1994).
19. H. G. Scott, *J. Appl. Crystallogr.* **16**, 159 (1983).
20. K. Oikawa, T. Kamiyama, F. Izumi, B. C. Chakoumakos, H. Ikuta, M. Wakihara, J. Li, and Y. Matsui, *Solid State Ionics* **109**, 35 (1998).
21. J. M. Tarascon, W. R. McKinnon, F. Coowar, T. N. Bowmer, G. Amatucci, and D. Guyomard, *J. Electrochem. Soc.* **141**, 1421 (1994).
22. A. Yamada, K. Miura, K. Hinokuma, and M. Tanaka, *J. Electrochem. Soc.* **142**, 2149 (1995).
23. W. R. Busing, K. O. Martin, and H. A. Levy, Report ORNL-TM-306, Oak Ridge National Laboratory, Oak Ridge, TN, 1964.
24. R. D. Shannon, *Acta Crystallogr. A* **32**, 751 (1976).
25. P. Thompson, D. E. Cox, and J. B. Hastings, *J. Appl. Crystallogr.* **20**, 79 (1987).
26. C. J. Howard, *J. Appl. Crystallogr.* **15**, 615 (1982).
27. R. A. Young and P. Desai, *Arch. Nauk. Mater.* **10**, 71 (1989).
28. A. C. Larson and R. B. Von Dreele, "GSAS, General Structure Analysis System," LAUR 86-748, Los Alamos National Laboratory, Los Alamos, NM, 1990.
29. C. Sigala, D. Guyomard, A. Verbaere, Y. Piffard, and M. Tournoux, *Solid State Ionics* **81**, 167 (1995).
30. A. Yamada, D.Eng. thesis, University of Tsukuba, Tsukuba, Japan, 1996.